



JPL Document D-93064

**TECHNOLOGY DEVELOPMENT
FOR EXOPLANET MISSIONS**
Technology Milestone Report

**Phase-Induced Amplitude Apodization (PIAA) Technology
Development, Milestone 3**
10% Bandpass Contrast Demonstration

Olivier Guyon (PI)

University of Arizona

Brian Kern (Co-I), Jet Propulsion Laboratory

Andreas Kuhnert, Albert Niessner

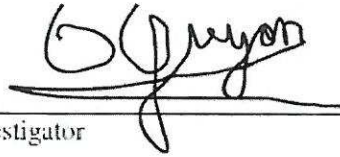
20 May 2014

National Aeronautics and Space Administration
Jet Propulsion Laboratory
California Institute of Technology
Pasadena, California

Reference herein to any specific commercial product, process, or service by trade name, trademark, manufacturer, or otherwise, does not constitute or imply its endorsement by the United States Government or the Jet Propulsion Laboratory, California Institute of Technology.

APPROVALS

Released by



May 20, 2014

Olivier Guyon, Principal Investigator
University of Arizona

Approved by



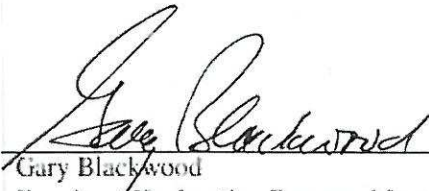
May 21, 2014.

Peter R. Lawson
Exoplanet Exploration Program Chief Technologist, JPL



5/22/14

Nicholas Siegler
Exoplanet Exploration Program Technology Manager, JPL



5/22/14

Gary Blackwood
Exoplanet Exploration Program Manager, JPL



6/23/14

Douglas Hudgins
Exoplanet Exploration Program Scientist, NASA HQ



6/23/14

John Gagosian
Exoplanet Exploration Program Executive, NASA HQ

LIST OF ACRONYMS

CCD	charge-coupled device
CLOWFS	coronagraphic low-order wavefront Sensor
DM	deformable mirror
HCIT	High Contrast Imaging Testbed
IWA	inner working angle
JPL	Jet Propulsion Laboratory
OAP	off-axis parabola
PIAA	phase-induced amplitude apodization
PIAA-CMC	PIAA complex mask coronagraph
PSF	point spread function
SAT	Strategic Astrophysics Technology
TDEM	Technology Development for Exoplanet Missions
TPF-C	Terrestrial Planet Finder Coronagraph
TRL	technology readiness level

TABLE OF CONTENTS

1. ABSTRACT.....	1
2. INTRODUCTION	1
2.1. Definition and significance of milestone	1
2.2. Technical approach	2
3. EXPERIMENT CONFIGURATION AND TECHNIQUE	3
3.1. Optical layout.....	3
3.2. Off-axis distances.....	5
3.3. Image reduction and photometric normalization	5
4. MILESTONE SPECIFICATION	8
4.1. Success Criteria.....	8
4.2. Validation Procedure	9
4.3. Certification Data Package.....	9
5. RESULTS	10
5.1. Model predictions	10
5.2. Description of contrast results.....	10
5.3. Histograms of intensity measurements	11
5.4. Additional reference information.....	11
5.4. Further analysis of intensity data: Radial scatter plots.....	12
6. CONCLUSIONS.....	13
Appendix 1. Calculation of λ_0/D_{sky}	15
REFERENCES	15

1. ABSTRACT

This report describes the progress reached toward Milestone 3 of the Phase-Induced Amplitude Apodization (PIAA) Technology Development experiment, funded under a NASA 2010 Technology Development for Exoplanet Missions grant. PIAA Milestone 3 is a demonstration of 10% spectral bandpass coronagraphic starlight suppression at small inner working angles, at contrast levels relevant for a space-based exoplanet imaging mission. The milestone is a requirement to “Demonstrate using Phase-Induced Amplitude Apodization a baseline contrast averaging 10^{-9} between a $2 \lambda/D$ inner working angle and a $4 \lambda/D$ outer working angle, in light at a wavelength in the range of $400 \text{ nm} \leq \lambda \leq 900 \text{ nm}$ with a 10% fractional bandpass.”

This document describes the scientific basis for targeting 10^{-9} contrasts in a coronagraph and the relevance of small inner working angles, the hardware comprising this coronagraph, and the results obtained. The results demonstrate 10^{-8} mean contrast, shown in Fig. 1. The milestone requirements were not met, but the achieved results are described in detail in this report. In addition, the results of a relevant published model, which predicts a similar contrast limit, are discussed; they imply that the contrast would improve if the amplitude errors (due to surface errors on the PIAA mirrors) were reduced, although this model has not been confirmed independently.

2. INTRODUCTION

2.1. Definition and significance of milestone

In support of NASA’s Exoplanet Exploration Program and under the Strategic Astrophysics Technology (SAT), Technology Development for Exoplanet Missions (TDEM) funding program, our team has been advancing the Technology Readiness Level (TRL) for the PIAA starlight suppression technique. The purpose of the PIAA Milestone 3 (10% broadband contrast demonstration at $2 \lambda/D$), the methodology for computing the milestone metric, and the success criteria against which the milestone are evaluated, are described in detail in the PIAA Milestone 3 white paper [1].

This milestone addresses broadband starlight suppression at small inner working angles with a PIAA

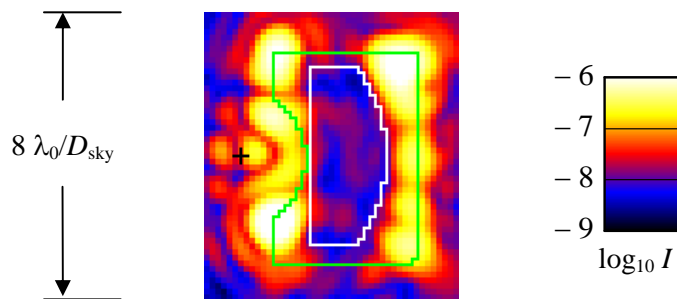


Fig. 1. Measured coronagraphic image showing dark hole with mean intensity 10^{-8} in a 10% bandpass. The field of view is $8 \lambda_0/D_{\text{sky}}$ on each side. Intensities are normalized to the occulter-out peak. The source center is marked with a small black cross, and the “scored” region border with inner edge at $x = 2 \lambda_0/D_{\text{sky}}$, outer radius $4 \lambda_0/D_{\text{sky}}$, is shown in white. The green line marks the edge of the occulter, the boundary between being fully opaque and fully transmitting.

coronagraph, a high-efficiency coronagraphy technique enabling high-contrast imaging at a small inner working angle ($\sim 2 \lambda/D$ for the configuration to be tested for this milestone) [2-11]. This milestone demonstration was performed on an optical table including key elements of any future high contrast imaging instrument for a future space mission (deformable mirror, science camera, coronagraph optics and active wavefront control), and is therefore of high relevance for direct imaging of exoplanets and disks from space.

Thanks to its high throughput, good angular resolution and small inner working angle (IWA), PIAA allows detection and characterization of habitable planets with a smaller telescope than was originally thought to be required [12-13]. While the theoretical potential of the PIAA has been widely recognized and estimated in mission concept studies, the realization of PIAA in future missions awaits proof of technical readiness traceable to space-based exoplanet mission science requirements and implementation constraints. PIAA Milestone 3 is an important step in this direction, demonstrating key advantages of the approach (small IWA, high contrast, with a high-throughput, high angular resolution architecture). A numerical comparison of a “generalized” PIAA architecture to other general architectures is presented in Ref. 9, while a comparison of coronagraph laboratory test results (including those presented here) appears in Ref. 14. These comparisons highlight the advantages, and motivation, for developing PIAA.

2.2. Technical approach

PIAA is a lossless beam apodization technique. Beam apodization is very useful in coronagraphy: an apodized pupil produces a high contrast image free of Airy rings. The conventional method to apodize the pupil is to introduce in the beam a mask which is fully transmissive in the center and becomes opaque at the edge of the pupil. With PIAA, the same apodized pupil is created by geometric redistribution of the light rather than selective absorption. This is achieved by aspheric optics (mirrors or lenses), as illustrated in Fig. 2.

The Airy rings produced with a conventional imaging telescope are due to diffraction originating from the sharp edges of the pupil. Pupil apodization, by creating a soft-edged pupil, can therefore greatly reduce these rings, and can be used either by itself or in combination with other coronagraph techniques (for

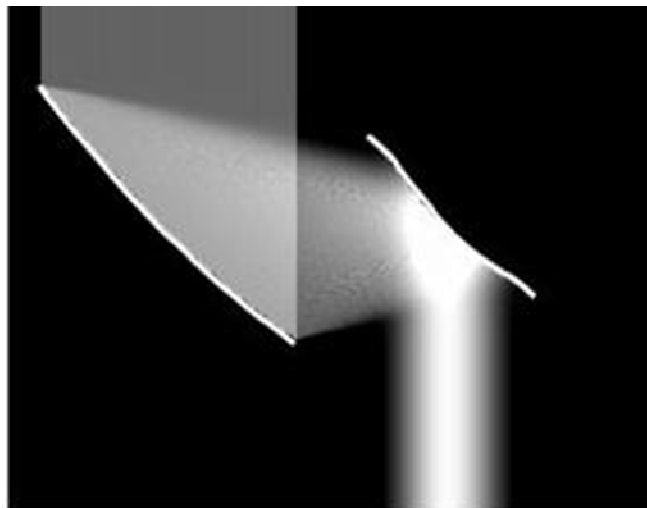


Fig. 2. PIAA uses aspheric optics to apodize a beam.

example, the apodized pupil Lyot coronagraph which combines pupil apodization with Lyot coronagraphy). The conventional technique used to apodize the telescope beam is with an amplitude mask (continuous or binary) with variable transmission from the center to the edge of the pupil. This leads to a difficult compromise between reaching high contrast (which requires a strong apodization) and achieving high coronagraph throughput and good angular resolution (which both favor a weak apodization).

With PIAA optics, strong apodizations can be achieved with no loss in throughput or angular resolution, enabling high contrast imaging at small angular separation from the optical axis with almost no loss in efficiency. The PIAA's inner working angle at high contrast ranges from $0.64 \lambda/D$ for an aggressive PIAA design to $2 \lambda/D$ for a more conventional PIAA design (design choice depends on the goal contrast, manufacturing capabilities, ability to mitigate chromatic issues and angular size of the central source). PIAA does not absorb light, and it therefore preserves the sensitivity and angular resolution of the telescope. The introduction of a Lyot stop, as explained below, results in a small decrease in throughput. When implemented with mirrors, PIAA can be made to operate at high contrast over a wide spectral band.

The performance gain offered by PIAA for detection and characterization of exoplanets over other coronagraphs is quantified in Ref. 9. Compared to the more conventional coronagraphs which were considered for the Terrestrial Planet Finder Coronagraph (TPF-C), adopting the PIAA is equivalent to a $2\times$ to $3\times$ gain in telescope diameter. Some PIAA-based concepts such as PIAACMC allow even higher performance, with high contrast detection of exoplanets closer in than $2 \lambda/D$ [11].

3. EXPERIMENT CONFIGURATION AND TECHNIQUE

3.1. Optical layout

The JPL High Contrast Imaging Testbed (HCIT) PIAA testbed has been conducting high-contrast imaging experiments since 2009 [15-17]. It uses the first generation of PIAA mirrors fabricated by Axsys [8]. A schematic representation of the optical train is shown in Fig. 3. The optics are mounted on a $5' \times 8'$ table that is placed in a vacuum chamber. The layout of the optics on the table is shown in Fig. 4. The vacuum chamber typically reaches pressures around 10^{-6} Torr.

The optical train begins outside of the vacuum chamber, with a Fianium SC-450 supercontinuum source, whose light passes through one of four bandpass filters, centered at 770, 790, 810, and 830 nm, each with a nominal 20 nm bandpass. This light is coupled into a single-mode fiber that passes through a vacuum feedthrough, and illuminates a pinhole at the source (at the left of Fig. 3). The light then passes through the PIAA mirrors, creating an apodized pupil at the output of PIAA M2, with a nominally spherical wavefront. The PIAA M2 is relayed to a pupil stop (a circular aperture), and then relayed again to the deformable mirror (DM), a 32×32 -actuator Xinetics electrostrictive DM, with a 1 mm actuator pitch and a gold-coated continuous face sheet. The source is then imaged onto the occulter, recollimated and passed through a Lyot stop (another circular aperture, $D_{\text{Lyot}}/D = 0.60$), and reimaged onto the camera. The camera can translate farther downstream to a location conjugated to the pupil stop (and to PIAA M2, the DM, and the Lyot stop). A linear polarizer is in place at the camera, so all images represent a single linear polarization state. The entire system, with the exception of the supercontinuum light source, is unchanged from its use in the Milestone #1 experiment [18].

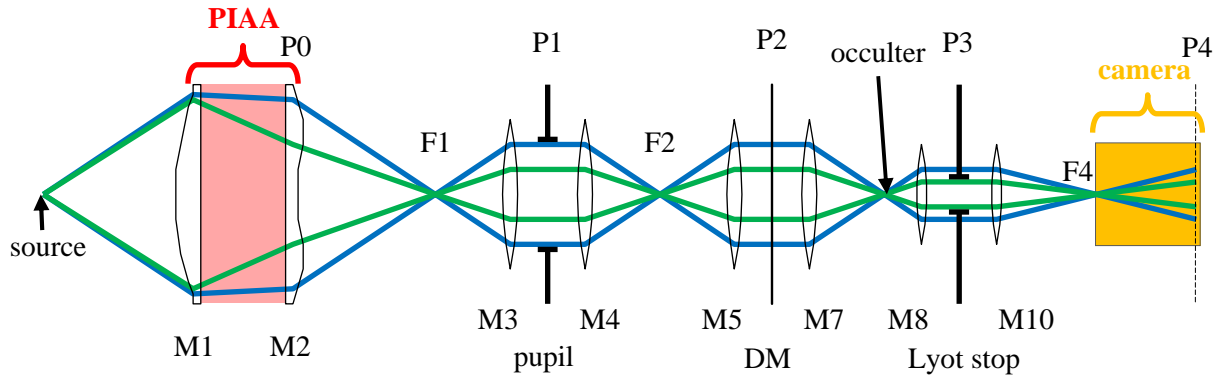


Fig. 3. Unfolded optical train to the science camera, not to scale. The marginal rays defined by the pupil stop (P1) are shown in blue, the marginal rays defined by the Lyot stop (P3) are shown in green. The planes conjugate to the source are easily identified as the locations where marginal rays cross; the occulter lies in a plane conjugate to the source. The planes conjugate to the pupil stop (P1) are labeled P0 – P4, and include PIAA M2 (P0), the DM (P2), and the Lyot stop (P3). The science camera is mounted on a translation stage that can reach a plane conjugate to the source (F4) and, by translating downstream, a plane conjugate to the pupil (P4), a range shown here in gold. The source and occulter can each be moved in 3 dimensions, and the pupil stop and Lyot stop can be removed. The CLOWFS system is not shown in this figure.

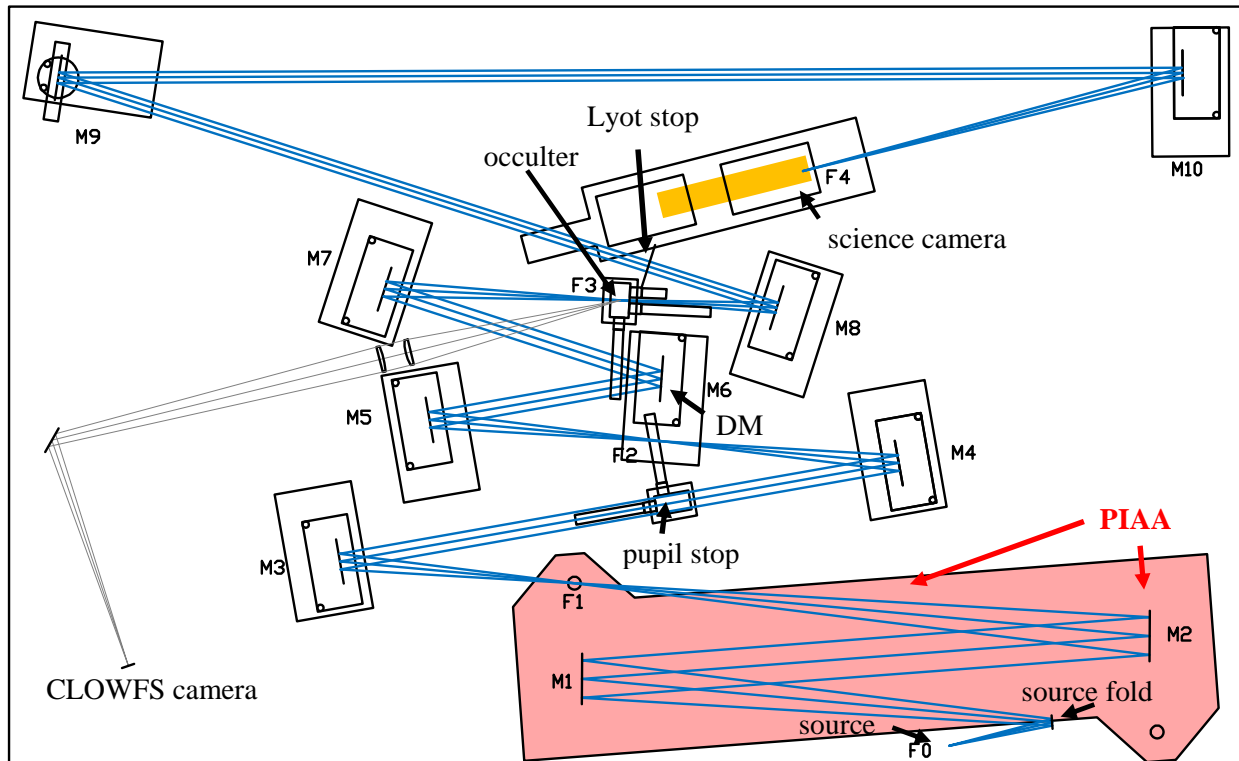


Fig. 4. Layout of optics on table, to scale. The source is at the bottom-right (F0). Light reflected off the occulter (gray rays) is relayed to the CLOWFS camera (bottom left). M9 is a flat mirror. The source fold mirror and DM have piezo actuators for tip-tilt (used by CLOWFS).

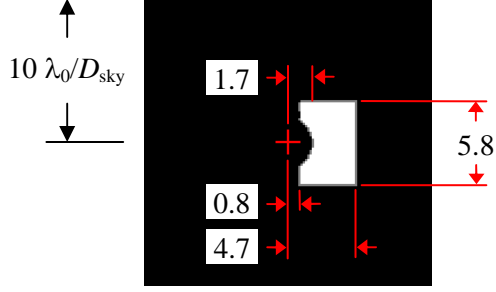


Fig. 5. Occulter transmission. This transmission is measured at the science camera, ranging from 0 to 1, seen with the Lyot stop removed. The occulter is positioned so that the source image is centered on the red cross at the center of this image. The full image is $\pm 10 \lambda_0/D_{\text{sky}}$ on each side (wider than in Fig. 1). The dimensions of the mask parameters are shown in λ_0/D_{sky} units, defined in Sec. 3.2. The inner radius is $1.7 \lambda_0/D_{\text{sky}}$, while the farthest corners are located at $5.5 \lambda_0/D_{\text{sky}}$ (quadrature sum of $x = 4.7$ and $y = 2.9$).

A transmission image of this occulter (the light that passes through to the science camera) is shown in Fig. 5. The occulter is freestanding, in the sense that there is no substrate in the region where transmission occurs; the transmission of 1 is through a region of vacuum. The inner radius of the transmitting region is $1.7 \lambda_0/D_{\text{sky}}$, where λ_0/D_{sky} is defined in Section 3.2 below.

3.2. Off-axis distances

Because PIAA optics are not first-order optics, off-axis distances in conjugate planes experience an additional magnification that is unrelated to the Lagrange invariant. This is essentially due to the fact that the marginal rays pass through PIAA optics differently than the rays carrying the bulk of the intensity. Conjugate points are no longer located at the same multiples of (λ/D) or $(f\lambda/D)$.

To scale image planes in a manner relevant to the on-sky angles, all off-axis distances in this study will be quoted in units of λ_0/D_{sky} , which is defined by:

$$\lambda_0/D_{\text{sky}} = \begin{cases} f\lambda_0/D, & \text{image planes upstream of PIAA,} \\ Mf_0\lambda/D, & \text{image planes downstream of PIAA,} \end{cases}$$

where (f/D) is assumed to be $2/\tan \theta_m$, with θ_m the angle between marginal and chief rays, and the nominal center wavelength $\lambda_0 = 800$ nm. The M introduced here is the remapping magnification, described below. Using these expressions, λ_0/D_{sky} represents positions on the sky as would be seen by a telescope feeding the coronagraph, appropriate to the locations where planets would be imaged. All locations are scaled using the center wavelength of the 10% band, *i.e.*, only a single λ_0 is used.

The measurements that went into the calculation of λ_0/D_{sky} , measured in pixels, are explained in Appendix 1 (with reference to Milestone #1), giving an answer of $1 \lambda_0/D_{\text{sky}} = 6.28$ pix.

3.3. Image reduction and photometric normalization

As images are read off of the science camera, they are first bias- and dark-subtracted. The bias level is read from a region of charge-coupled device (CCD) overscan, in each image. The dark field calibration

involves taking images in which the shutter is not activated, to produce a dark reference frame, which is then subtracted from the bias-subtracted CCD images. The mean dark level relevant to dark hole intensity measurements typically amounts to 10^{-10} , and the dark reference frames are measured to vary over month timescales by less than 10^{-11} , so errors in the dark subtraction are estimated to be less than 10^{-11} .

All intensity measurements relevant to the coronagraph are normalized to the occulter-out, Lyot-in intensity peak, separately for each spectral channel. The process of referencing coronagraphic images with intensities well below 10^{-9} , to occulter-out images with intensity at 1.0, is done in three stages, with each stage spanning approximately 10^3 in dynamic range. In each case, a 10^3 dynamic range in an individual scene is used to relate intensities to the next stage, with the exposure times increasing by 10^3 between stages. Fig. 6 gives a schematic representation of the 3-stage photometric normalization chain, for a single spectral channel.

The first two stages, taken together, establish the normalized intensity of a pre-defined photometric reference region (shown in green in the center and right panels of Fig. 6), near 10^{-6} . This sequence is repeated infrequently (before and after each experiment, typically). With the reference region calibrated, every successive coronagraph image (the right-hand panel of Fig. 6) is scaled in intensity so that the reference region matches its calibrated intensity. In this way, every coronagraph image is “locally” normalized, making the final answers insensitive to source throughput variations or to calibration of exposure time linearity.

The reference region itself is chosen to capture light that “leaks” through a defect in the occulter. This is a low-transmission sliver reaching through the outer PSF (located $\sim 9 \lambda_0/D_{\text{sky}}$ above the source image). The source PSF landing in this location (see the right panel of Fig. 6) is affected very little by DM changes (the Nyquist condition on the DM corresponds to $6 \lambda/D_{\text{sky}}$). However, before correction (see center-right panel of Fig. 7), light passing through the main opening of the occulter is diffracted by the Lyot stop to overlap the reference region; after this light is removed by wavefront control (compare to bottom-right panel of Fig. 7), the light falling in the reference region decreases by $\sim 10\%$, and the reference region needs to be re-calibrated.

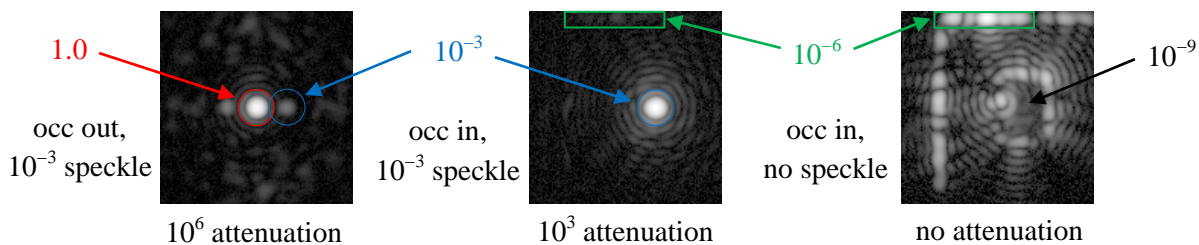


Fig. 6. Three stages of photometric normalization. (LEFT) Stage 1, remove occulter, add 10^{-3} speckle using DM, measure ratio of star (1.0) to speckle ($\sim 10^{-3}$). (CENTER) Stage 2, replace occulter, measure ratio of speckle ($\sim 10^{-3}$) to reference region (in green, $\sim 10^{-6}$). (RIGHT) Stage 3, remove speckle, scale entire image so that reference region brightness matches stage 2. Each stage involves intra-scene ratios with dynamic range $\sim 10^3$, with source attenuation decreasing by 10^3 between stages. Each panel is $\pm 10 \lambda_0/D_{\text{sky}}$ on each side, log-scaled. The Lyot stop is in for all stages.

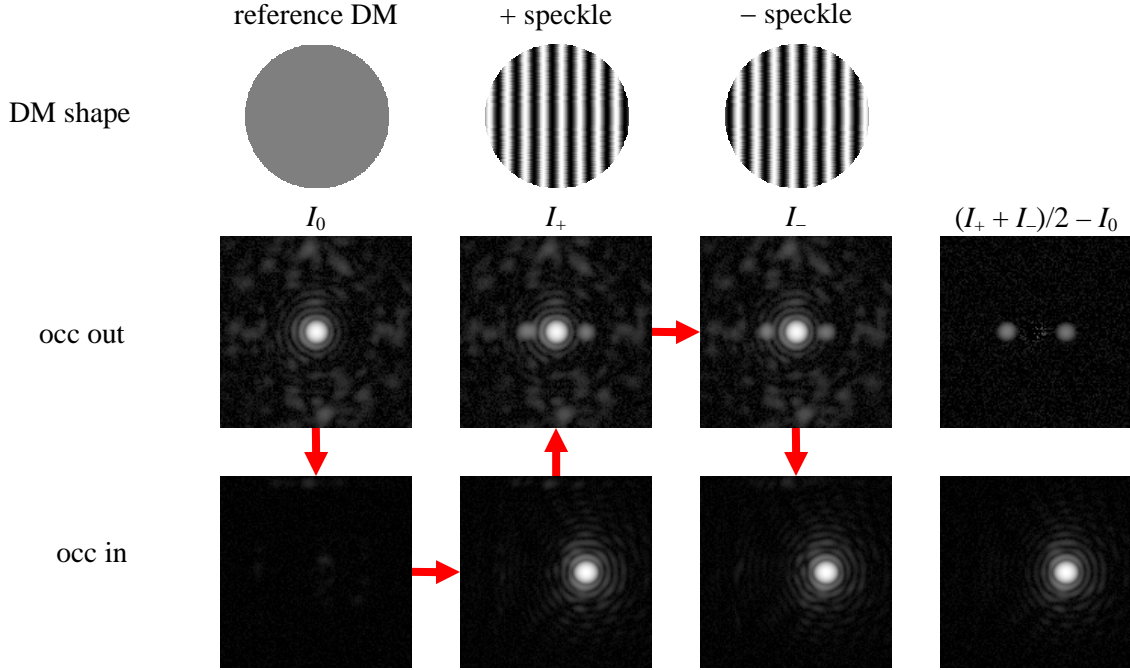


Fig. 7. Speckle ratio measurement sequence. Images are taken in the order directed by the red arrows, first by alternating occulter out / in (with source attenuation different by $\sim \times 10^3$), then by modulating the DM to add a positive and negative speckle. The calculation in the right-hand column represents only the “AC-coupled” term, i.e., the speckles alone. The right-hand speckle of the “occ out” row is the same normalized brightness as that of the “occ in” row. This process is repeated separately for each spectral channel.

In practice, the reference region is calibrated for each spectral channel before wavefront control to provide an initial approximate normalization for real-time use, then after wavefront control has completed, the reference region is re-calibrated using the final wavefront, and all previously acquired images are re-normalized to take on their final values. This post-processing normalization accommodates both changes in the PSF landing on the occulter leak itself, and changes in the light diffracted from the main opening of the occulter by the Lyot stop.

The relationship between calibration stages 1 and 2 is established by introducing a 10^{-3} speckle, done by adding a sinusoid to the DM. The calibration sequence relies on this speckle being the same in stage 1 as in stage 2. This is accomplished by taking a series of images for each stage, one image before changing the DM, one image with a sinusoid added, and a third image with the same sinusoid subtracted. Analyzing the three-image sequence allows the speckle intensity to be measured “AC-coupled,” i.e., with no influence from the underlying E -field (which is different with and without the occulter present).

As is shown in Fig. 7, by measuring the I_0 , I_+ , and I_- images, corresponding to the addition of a “+” and a “-” speckle, the speckles can be isolated from I_0 by calculating $(I_+ + I_-)/2 - I_0$. The brightness of the occ out speckle is the same as the brightness of the occ in speckle (with $\ll 1\%$ effect from propagation through the occulter and Lyot stop), allowing stage 1 and stage 2 to be calibrated to each other (see Fig. 6).

The important thing to note about this construction is that there is no reliance on stability of the light source, or on repeatability or linearity of the exposure times, or on any assumption about the input spectrum. During normal operation, every frame contains a measurement of the reference region, so that this normalization implicitly accommodates any combination of source brightness, spectral, exposure time or throughput variability. The specific calibration sequence, taken in 3 steps (see Fig. 6), involves the addition of a dynamic speckle to transition from stage 1 to stage 2, rather than trying to span a 10^6 dynamic range in one transition (without any common intra-scene reference).

The 10% bandpass for this experiment is constructed from four 2.5% bandpasses (spectral channels), each observed sequentially. The individually normalized intensities of the spectral channels are averaged to estimate the intensity in a 10% bandpass. A sample sequence of four bandpass images is shown in Fig. 8, on the left. In this way, all analysis is relative to a synthetic “flat” spectrum, regardless of the input spectrum shape. During wavefront control iterations, following the contrast evaluation, a sequence of DM probe shapes is applied, observed in each of the four bandpasses, to be used for wavefront estimation, as shown in Fig. 8.

4. MILESTONE SPECIFICATION

The milestone success criteria, validation procedure, and certification package are described in the white paper, and are duplicated here in abridged form, with minor wording and notation changes. Any significant differences with respect to the original definitions are identified in italics, and separate notes are set in brackets. Note that the section numbers are referenced to this document, and so will not match individual section numbers in the white paper.

4.1. Success Criteria

4.1.1. A set of filters shall be used to discretely sample the full 10% FWHM wavelength range. Contrast values obtained with these filters shall be averaged to determine the broadband contrast over a 10% or greater bandwidth. Single or dual polarization light will be used at a central wavelength in the range of

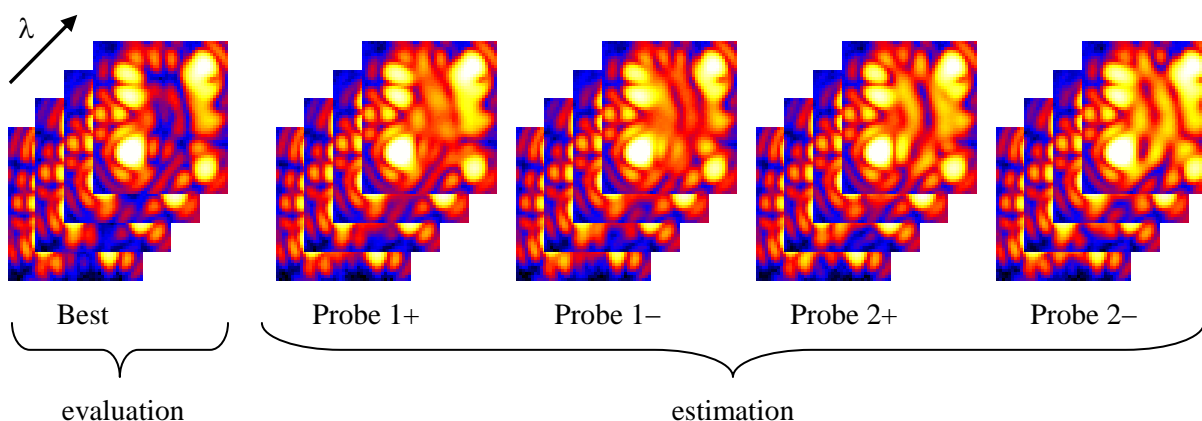


Fig. 8. Images acquired for one iteration. For the initial DM setting (“best”), an image is taken in each spectral channel to evaluate the mean contrast. A sequence of four probe shapes are put on the DM, and for each probe shape, an image is taken in each spectral channel. These are combined to form the wavefront estimate that determines the following iteration’s initial DM setting.

400 nm < λ < 900 nm.

Rationale: This approach is required to correct for spectral variations in the supercontinuum light source, a problem that will not be encountered with real stars in a space mission.

[The center wavelength for this experiment was $\lambda_0 = 800$ nm. Four 2.5% filters were used, see Sec. 3.3. A single polarization state was analyzed.]

4.1.2. A mean contrast metric of 10^{-9} or smaller shall be achieved in a 2 to 4 λ_0/D dark zone.

Rationale: This provides evidence that the high contrast field is sufficiently dark (10^{-9} expected exozodi level) to be useful for searching planets, and test whether there is a fundamental limitation at the inner working angle.

[The mean intensity in the dark hole was 10^{-8} for this experiment. This criterion was not met.]

4.1.3. Criterion 4.1.2, averaged over the data set, shall be met with a confidence of 90% or better. Sufficient data must be taken to justify this statistical confidence.

[Since 4.1.2 was not met, 4.1.3 was also not met.]

4.1.4. Criteria 4.1.1 – 4.1.3 must be satisfied on three separate occasions with a reset of the wavefront control system software (DM set to scratch) between each demonstration.

[Since neither 4.1.2 nor 4.1.3 was met, 4.1.4 was also not met.]

4.2. Validation Procedure

4.2.1. DM is set to scratch.

4.2.2. Wavefront control iterations produce a high-contrast dark hole.

4.2.3. Each wavefront control iteration includes a measurement with the DM solution for best contrast. This measurement is used for all intensity analysis presented in this report.

4.3. Certification Data Package

4.3.1. Model predictions of contrast performance.

4.3.2. Calibrated images of the reference star.

4.3.3. The coronagraph transmittance profile and focal plane scale.

4.3.4. A set of contrast field images.

4.3.5. A contrast metric value for the target area in each of the contrast field images.

4.3.6. A statistical analysis of the contrast values, with the 90% confidence contrast value for the data set

4.3.7 A histogram of the brightness distribution of pixels in the dark field for each of the high contrast images in the data set, and for the combined data acquired in each data set.

5. RESULTS

5.1. Model predictions

Ref. 19 contains a detailed analysis of the expected broadband contrast performance of this particular configuration. The inputs to those models were the measured pupil-plane amplitude and phase from the testbed itself, with the same coronagraphic components as used here, which are categorized as the “C1” configuration with a “Circular-Stop” in the paper. A range of different Lyot stop sizes was simulated, and Fig. 9b of Ref. 19 shows the expected performance over a 7.5% bandpass, reaching between 1×10^{-8} and 2×10^{-8} . While the modeled bandpass was 7.5% and the experimental bandpass was 10%, the model numbers for $D_{\text{Lyot}}/D = 0.6$ are in approximate agreement with the testbed results of 10^{-8} (a rough factor of 2). A typical assumption would be that contrasts degrade as the square of the bandwidth, so the difference in the contribution of bandwidth between 7.5% and 10% would also be less than a factor of two, although in the sense that the 10% numbers should be worse than the 7.5% numbers (the opposite of the case here).

It should be noted that few models have calculated expected PIAA performance including high-order wavefront control, and Ref. 19 is the only published result applicable to the testbed. As such, there is no available cross-check on the applicability of that model. It should also be noted that there has not been established agreement between different models regarding contrast limits, so the results of any one model should not be interpreted to have any great confidence.

The analysis in Ref. 19 shows that much better contrasts would be obtained for smaller input pupil plane amplitude errors. The amplitude errors in the current system are predominately due to surface errors on PIAA M1, which generate amplitude errors through their Fresnel propagation to M2 (conjugated to the pupil stop). The Axsys PIAA mirrors, which were the first generation of PIAA mirrors to be fabricated, had looser tolerances on their surface errors than the second generation of PIAA mirrors. The next step in this investigation is to repeat the same testbed experiment using the second generation mirrors, to achieve better performance. This is discussed further in Section 6 below.

5.2. Description of contrast results

The wavefront control iterations stopped showing contrast improvement at a mean dark hole intensity of 1.00×10^{-8} . The results for each spectral channel, as well as the synthetic 10% bandpass, are shown graphically in Fig. 9 and in Table 1. What is clear is that there is less light in the central two spectral channels than in the outer two, and that there is strong evidence of ring structure in the outer two spectral channels.

The ring structure seen in the shortest and longest wavelength channels is likely due to the presence of the Lyot stop. The Lyot stop, and its corresponding discontinuous drop in amplitude, give rise to a

	$m_{770} \times 10^8$	$m_{790} \times 10^8$	$m_{810} \times 10^8$	$m_{830} \times 10^8$	$m_{10\%} \times 10^8$
Intensity	1.60	0.44	0.47	1.51	1.00

Table 1. Contrast results in individual spectral channels, and in synthetic 10% passband.

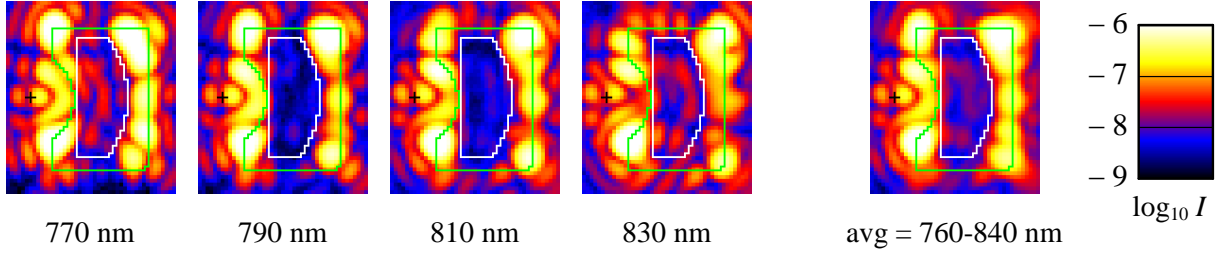


Fig. 9. Four individual spectral channel images, and the average of all four. Each spectral channel is 20 nm wide. Each image extends from -1 to $+6 \lambda_0/D_{\text{sky}}$ in x , $\pm 4 \lambda_0/D_{\text{sky}}$ in y . The black cross is the center of the source image, the green box is the edge of the occulter, the white box is the scored region of the dark hole.

diffraction pattern that shares some similarities with an Airy pattern, producing an E -field that oscillates positive and negative with radius, creating rings. These rings can be eliminated monochromatically by the wavefront control, but over a range of wavelengths they are more difficult to effectively suppress.

Because the contrast requirement set by the milestone white paper was not met, the statistical analysis of the margin by which it needs to be met does not have relevance. The proposed statistical analysis of a sequence of images was not done. The measurement noise alone, the combination of read noise and shot noise (dominated by shot noise) comes to about 6% for pixel at 10^{-8} in each spectral channel, or 3% for the 10% bandpass (average of 4 spectral channels). Averaging over 349 pixels in the dark hole, since the measurement noise is independent between pixels, leads to a measurement noise level below 0.2%, certainly below the calibration uncertainties. The calibration uncertainties, estimated in Milestone #1, were near the 2% level, so that can be adopted as the overall uncertainty in the 1.00×10^{-8} measured mean intensity.

5.3. Histograms of intensity measurements

Fig. 10 (following page) shows the histograms of measured intensity in each pixel of each spectral channel, as well as in the synthetic 10% bandpass. Again the most obvious feature is that the central two spectral channels are concentrated at low intensity values. None of the distributions look like Gaussian or Poissonian distributions, which is most likely due to spatial morphological variations, which do not produce a simple distribution when examined in this way.

5.4. Additional reference information

As specified in the milestone certification data package requirements, a calibrated image of the reference star (occulter-out, Lyot-in) is shown in Fig. 11 (following page), along with a coronagraph throughput plot. The coronagraph throughput shown is absolute, for the polarization state used in this experiment. Absolute coronagraph throughput in this context accounts only for light losses on the coronagraphic elements, *i.e.*, the occulting mask and Lyot stop, but not the reflectivities of the relay optics or the camera sensitivity.

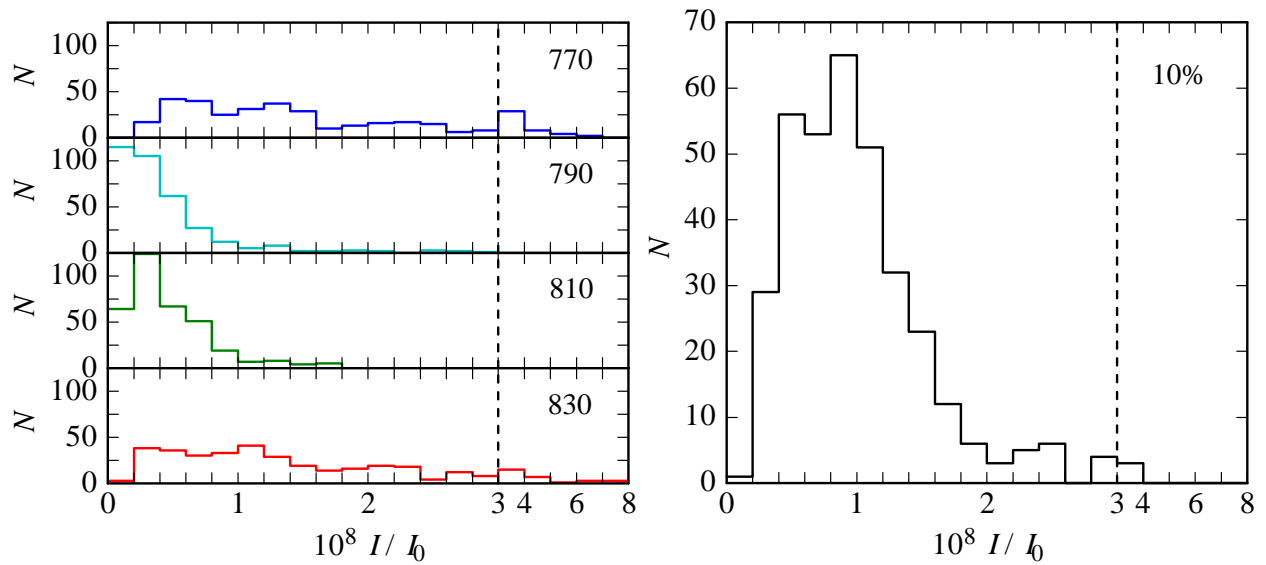


Fig. 10. Histograms of intensity values in dark hole. The left panel shows each of the four spectral channels separately, the right panel is the mean of all four spectral channels (the 10% bandpass). In every panel, there are 349 pixels in the dark hole, i.e., the sum of all histogram bin N values is 349. Note that the bin edges (horizontal axis values) are not uniform, the vertical dashed line shows the break in bin size spacing. All points are plotted (*i.e.*, there are no negative values and no values over 8×10^{-8}).

5.5. Further analysis of intensity data: Radial scatter plots

Another method to display the pixel-to-pixel variations is the scatter plots of intensity vs. radius in Fig. 12 (on the following page). The intensities are binned over 1 pixel in radius, which corresponds to $(1/6.28) \lambda_0/D_{\text{sky}}$ -sized bins.

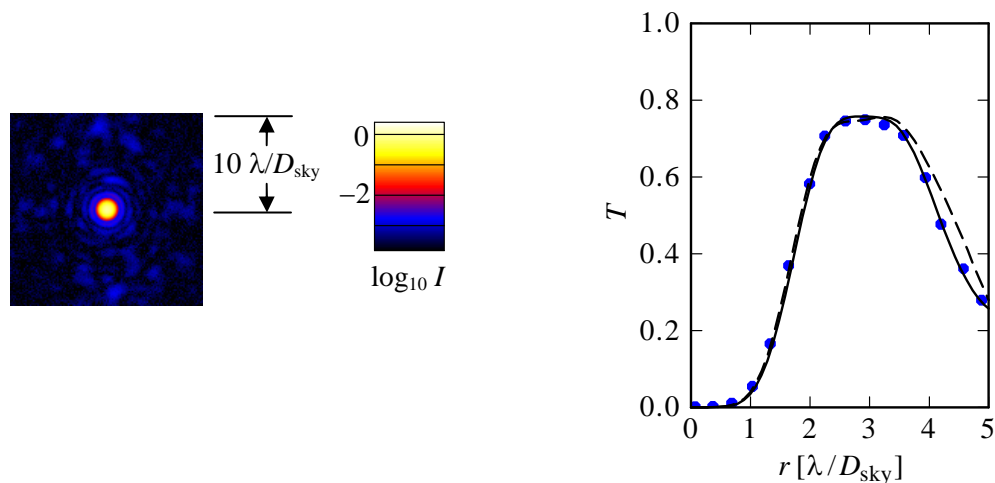


Fig. 11. (LEFT) Calibrated image of reference star, and (RIGHT) absolute coronagraph throughput.

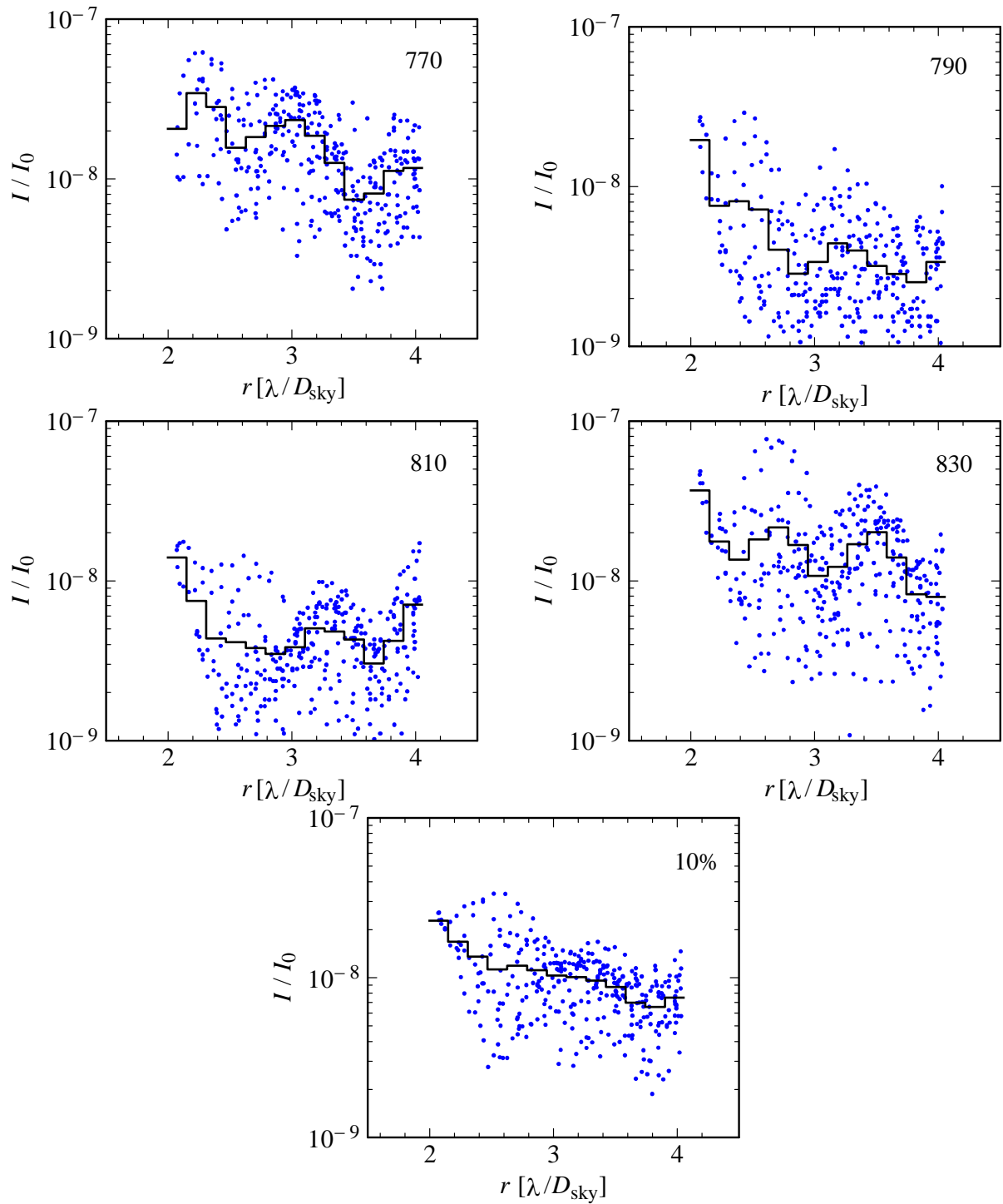


Fig. 12. Intensity vs. radius for four spectral channels, and for average of all four (10%). Each blue point is a single pixel from the 349 pixels inside the white box of Fig. 8. The solid black lines are binned averages, with bin width 1 pixel = $(1/6.28) \lambda_0/D_{\text{sky}}$.

6. FUTURE DIRECTION

As stated in Section 5.1, the models of Ref. 19 indicate that decreasing the amplitude errors in the pupil plane would allow better contrasts. This implies that the Axsys PIAA mirrors used here are the limiting component in the coronagraph. A second generation of mirrors, fabricated by Tinsley, have been installed onto the PIAA testbed. The Tinsley mirrors have tighter tolerances on surface errors than the Axsys mirrors (used in the experiment reported here), which translates to smaller amplitude errors, and a reduction in the limiting factor experienced here. A detailed analysis of the expected limiting contrast using the second generation of mirrors, given the Tinsley surface errors, has not been performed.

The modeling result indicating improved performance from reduced amplitude errors motivates the desire to replace the Axsys mirrors with Tinsley mirrors. Also, a programmatic plan is in place to exchange the Axsys and Tinsley mirrors, independent of the testbed results, based on mutual agreement between the JPL and Ames coronagraph testbeds.

In addition to the choice of specific coronagraph components in the current configuration, the decision was made to convert the coronagraph architecture to that of a PIAA-CMC, as described in Ref. 20. A PIAA-CMC coronagraph includes an occulter which allows careful optimization of the diffraction as a function of wavelength. One advantage of this configuration is that some modes of chromatic residual errors, whatever their origin, can be accommodated by changes in the occulter design. In the short term, the plan is to use only a small portion of the clear aperture of the Tinsley mirrors for the PIAA-CMC design (in the longer term, new mirrors will be fabricated). This further improves the standpoint with respect to wavefront errors, as the quality over just the center portion of the mirrors is better than over the entire clear aperture.

This approach to implementing improvements in the broadband contrast is two-fold, including both an improvement in the surface figure of the mirrors and the inclusion of a chromatic control in the occulting spot.

Separate from the model that indicated amplitude errors as a limit to the contrast, some inference may be made regarding the ring-like structure seen in Fig. 9, at the shortest and longest wavelengths. The likely source of this morphology would be diffraction at the edge of the Lyot stop, and its image-plane radial scaling with wavelength. How wavefront control interacts with this has not been adequately explored, and whether the net effect is significant compared to other contrast limits is not clear. In any case, further investigation into this particular effect is likely to be cut short by the switch to PIAA-CMC. While PIAA-CMC also has a Lyot stop, the nominal E -field amplitude is zero at the edge of the Lyot stop, so the ring-like structures should not form (or not to the same level) in PIAA-CMC.

7. CONCLUSIONS

The data described in this report demonstrate the combination of PIAA optical elements and wavefront control producing a 10% broadband dark hole with average intensity at the 10^{-8} level, at radii down to $2 \lambda_0/D_{\text{sky}}$. The details of the milestone requirements and the statistical analysis are presented in full, to validate the performance.

Appendix 1. Calculation of λ_0/D_{sky}

The complications of dealing with off-axis sources are explained in detail in the Milestone #1 writeup, in Sec. 3.2 and Appendix 2. Those analyses are not repeated here, but the technique for determining λ_0/D_{sky} is identical to that for λ/D_{sky} described in Appendix 2 of Milestone #1, except that $\lambda_0 = 800$ nm is used instead of the $\lambda = 807.5$ nm from the monochromatic Milestone #1. The result is $\lambda_0/D_{\text{sky}} = 6.28$, with the same conservative 2% uncertainty described in Milestone #1.

A separate check on the calibration of this number is provided by calibrating the speckle locations in all four spectral channels. The values, in $(\lambda/D)_{\text{cam}}$ (“system” units, not referenced to off-axis source locations), are $(\lambda/D)_{\text{cam}} = 2.334, 2.378, 2.477, \text{ and } 2.500$ pix. Each of these numbers is measured in an entirely independent way, so the residuals after a linear fit w.r.t. λ provide an estimate of the random errors in this determination. The random error estimated from fit residuals is 0.9%, smaller than the conservative 2% uncertainty chosen for this value.

REFERENCES

- [1] Guyon, O. et al. 2014, “Phase-Induced Amplitude Apodization Coronagraph: Broadband Contrast Demonstration,” <http://exep.jpl.nasa.gov/technology/>
- [2] Guyon, O. 2003, “Phase-induced amplitude apodization of telescope pupils for extrasolar terrestrial planet imaging,” *A&A*, **404**, 379.
- [3] Traub, W.A. and Vanderbei, R.J. 2003, “Two-Mirror Apodization for High-Contrast Imaging,” *ApJ* **599**, 695.
- [4] Vanderbei, R.J., Traub, W.A. 2005, “Pupil Mapping in Two Dimensions for High-Contrast Imaging,” *ApJ*, 626, 1079.
- [5] Guyon, O., Pluzhnik, E.A., Galicher, R., Martinache, F., Ridgway, S.T., Woodruff, R.A. 2005, “Exoplanet Imaging with a Phase-induced Amplitude Apodization Coronagraph. I. Principle,” *ApJ* **622**, 744.
- [6] Martinache, F., Guyon, O., Pluzhnik, E.A., Galicher, R., Ridgway, S.T. 2006, “Exoplanet Imaging with a Phase-Induced Amplitude Apodization Coronagraph. II. Performance,” *ApJ* **639**, 1129.
- [7] Vanderbei, R.J. 2006, “Diffraction Analysis of Two-dimensional Pupil Mapping for High-Contrast Imaging,” *ApJ* **636**, 528.
- [8] Pluzhnik, E.A., Guyon, O., Ridgway, S.T., Martinache, F., Woodruff, R.A., Blain, C., Galicher, R. 2006, “Exoplanet Imaging with a Phase-Induced Amplitude Apodization Coronagraph. III. Diffraction Effects and Coronagraph Design,” *ApJ* **644**, 1246.
- [9] Guyon, O., Pluzhnik, E.A., Kuchner, M.J., Collins, B., Ridgway, S.T. 2006, “Theoretical Limits on Extrasolar Terrestrial Planet Detection with Coronagraphs”, *ApJSS* **167**, 81.
- [10] Lozi, J., Martinache, F., Guyon, O. 2009, “Phase-Induced Amplitude Apodization on centrally obscured pupils: design and first laboratory demonstration for the Subaru Telescope pupil,” *PASP* **121**, 1232.
- [11] Guyon, O., Martinache, F., Belikov, R., Soummer, R. 2010, “High Performance PIAA Coronagraphy with Complex Amplitude Focal Plane Masks”, *ApJSS* **190**, 220.
- [12] PECO website: <http://zero.as.arizona.edu/CAAO/PECO/>

- [13] Levine, M. et al. 2009, “Levine, M., et al. 2009 Terrestrial Planet Finder – Coronagraph (TPF-C) Flight Baseline Mission Concept”, white paper provided to the 2010 Decadal Survey.
- [14] Lawson, P. R. et al. 2013, “Survey of experimental results in high-contrast imaging for future exoplanet missions,” Proc. SPIE **8864**, 88641F.
- [15] Kern, B., Give’on, A., Kuhnert, A., Levine-West, M.B., McMichael, I., Moody, D.C., Niessner, A.F., Pueyo, L., Shaklan, S.B., Traub, W.A., Trauger, J.T., Belikov, R., Guyon, O. 2009, “Phase-induced amplitude apodization (PIAA) coronagraph testing at the High Contrast Imaging Testbed,” Proc. SPIE **7440**, 74400H.
- [16] Kern, B., Give’on, A., Kuhnert, A., Niessner, A., Guyon, O. 2011, “Laboratory testing of a Phase-Induced Amplitude Apodization (PIAA) coronagraph,” Proc. SPIE **8151**, 815104.
- [17] Kern, B., Guyon, O., Kuhnert, A., Niessner, A., Martinache, F., Balasubramanian, K. 2013, “Laboratory demonstration of Phase Induced Amplitude Apodization (PIAA) coronagraph with better than 10^{-9} contrast,” Proc. SPIE **8864**, 88640R.
- [18] Guyon, O., Kern, B., Kuhnert, A., Niessner, A., Balasubramanian, K. 2014, “Phase-Induced Amplitude Apodization (PIAA) Technology Development, Milestone 1: Monochromatic Contrast Demonstration,” <http://exep.jpl.nasa.gov/technology/>
- [19] Sidick, E., Kern, B., Kuhnert, A., Shaklan, S. 2013, “Comparison of Simulated Contrast Performance of Different Phase Induced Amplitude Apodization (PIAA) Coronagraph Configurations,” Proc. SPIE **8864**, 88641Y.
- [20] Guyon, O. 2013 “Imaging Earth-like planets around late-type stars with low-inner working angle PIAA coronagraphy,” Proc SPIE **8864**, 8864414.